Case Studies in Thermal Engineering 27 (2021) 101311

Contents lists available at ScienceDirect

Case Studies in Thermal Engineering

journal homepage: www.elsevier.com/locate/csite

CFD modelling of the ammonia vapour absorption in a tubular bubble absorber with $NH_3/LiNO_3$

Andrés Zapata, Carlos Amaris *, Alexis Sagastume, Andrés Rodríguez

Universidad de la Costa, Energy Department, Cl. 58 #55-66, 080002, Barranquilla, Colombia

HIGHLIGHTS

- Development of a 3D CFD bubble absorber model using the $NH_3/LiNO_3$ solution.
- Detailed methodology for the CFD development and validation.
- Heat and mass transfer per area parameters required for mesh test and validation.
- The CFD model adequately reproduces the experimental data.

ARTICLE INFO

Keywords:
CFD
Heat and mass transfer
Absorption refrigeration system
Bubble absorber
Ammonia
Lithium nitrate

ABSTRACT

The absorber is a key component of absorption cooling systems, and its further development is essential to reduce the size and costs and facilitate the diffusion of absorption cooling systems. Computational fluid dynamics (CFD) can facilitate the characterization of the equipment used in absorption cooling systems at lower costs and complexity, but they must be properly developed and validated to provide reliability.

This study provides a detailed description and assessment of a 3D CFD bubble absorber model developed to simulate the absorption process in a vertical double pipe with the $NH_3/LiNO_3$ solution. It includes a comprehensive methodology to develop the CFD model and its validation considering the effect of the solution flow and the cooling water temperature on absorber performance parameters such as the absorption mass flux and the solution heat transfer coefficient. The results show that the 'Volume of Fluid model' and the 'Realizable k-epsilon model' provide the lowest residuals and computational times in the simulations while a good correspondence between the CFD model and the experimental data with errors below 10% and 7% for the absorption mass flux and solution heat transfer coefficient, respectively, was obtained. The maximum absorption rate and heat transfer coefficient were 0.00441 kg m^{-2} s^{-1} and 786 W m^{-2} K^{-1}, respectively.

1. Introduction

Vapour absorption refrigeration systems (VARs) are recognized as important alternatives to the traditional vapour compression systems, based on the possibility of using solar thermal energy [1–3] or residual heat [4–6] as energy input. This approach can reduce the environmental impacts associated to the high electricity consumption of vapour compression systems and increase the use of environmentally friendly working fluids. However, absorptions systems are still non-competitive with mechanical compression

* Corresponding author.
E-mail address: Camaris5@cuc.edu.co (C. Amaris).

https://doi.org/10.1016/j.csite.2021.101311
Received 24 June 2021; Received in revised form 31 July 2021; Accepted 3 August 2021
Available online 11 August 2021
2214-157X/© 2021 The Authors. Published by Elsevier Ltd. This is an open access article under the CC BY-NC-ND license (http://creativecommons.org/licenses/by-nc-nd/4.0/).

systems in term of size and costs, requiring further developments to address these disadvantages towards a widespread used at global scale.

The basic VARs consist of an absorber, a generator, a solution pump, a condenser, an expansion device, and an evaporator. Given the complex heat and mass transfer processes taking place in absorbers and desorbers, they are acknowledged as key components for VARs [7–9]. Therefore, understanding of the behaviour of these components is of the essence to improve the global performance of VAR systems.

Different studies have implemented various strategies to improve the performance of absorbers [10]. Depending on the operation mode, absorbers can be classified as bubble absorber, falling film absorber, adiabatic absorber, and membrane absorber. Particularly, bubble absorbers provide higher heat and mass transfer coefficients as compared to falling film absorbers [11,12]. Studies assessing absorbers can be classified as experimental/visual and numerical studies [13,14]. Experimental studies imply the design of complex and costly experimental test facilities to characterize the bubble absorption process. In several cases, the design of the test facility and its associated cost hinder the reproducibility of the experiments. On the other hand, numerical and theoretical studies have been highlighted as useful alternatives to facilitate a comprehensive understanding of the variables affecting the heat and mass transfer processes for various binary fluids [15–20], as it is the case of studies on the flow characteristics and bubble formation in absorbers showing that the limiting resistance for heat transfer is usually in the binary fluid side [15]. Moreover, the mass transfer has been found to decrease along the absorber as the solution approaches the equilibrium conditions [17]. Furthermore, the solution mass flow, solution mass fraction, solution temperature, heat dissipation temperature, hydraulic diameter, and length of the absorber were found to have stronger effects on the vapour absorption than on the vapour phase conditions [10].

In terms of working fluids, the $NH_3/LiNO_3$ solution appears as a promising alternative to overcome the limiting aspects of the conventional NH_3/H_2O and H_2O/LiBr solutions used in absorption refrigeration systems [21,22]. Some advantages of the $NH_3/LiNO_3$ solution, includes eliminating the vapour rectification after the generator, which permits lower driving temperatures contrasted to NH_3/H_2O absorption systems. Additionally, there is no risk of crystallization at the regular operating conditions for air-cooled absorption systems in warn environments as compared to H_2O/LiBr absorption systems. However, the high viscosity of $NH_3/LiNO_3$ solution has been found to limit the heat and mass transfer during the absorption process contrasted to the use of NH_3/H_2O solution [23,24]. Therefore, it is required to improve the heat and mass transfer processes in absorbers and generators using $NH_3/LiNO_3$ to development competitive $NH_3/LiNO_3$ absorption systems [25,26].

While there is a need to further study $NH_3/LiNO_3$ absorption systems, little numerical studies assessing the operation of absorbers with $NH_3/LiNO_3$ are available in literature [4,27,28]. A numerical model of a vertical tubular absorber for $NH_3/LiNO_3$ and NH_3/NaSCN solutions is reported [27]. To develop the model, the Nusselt's and penetration theories were implemented to simulate the heat and mass transfer in the desorber, contrasting the results with experimental data. The results showed mass transfer coefficients deviations ranging from 0.64 to 1.60 times the experimental data. Moreover, a theoretical model of a plate absorber was developed to compare the temperatures and thermal load profiles along the absorber operating with the NH_3/H_2O, $NH_3/LiNO_3$, and NH_3/NaSCN solutions [28]. Results indicated that the $NH_3/LiNO_3$ provided the lowest mass transfer and heat flow in comparison to the others two solutions due to its high viscosity. Moreover, Amaris et al. [29] reported empirical heat and mass transfer correlations and artificial neural networks-based models to assess the absorption process in a plate absorber with $NH_3/LiNO_3$. In this case, the authors reported absorption mass flux and heat flow with maximum errors of 10.8% and 11.3%, respectively, with respect to the experimental data.

The computational fluid dynamics (CFD) is an innovative and powerful numerical modelling approach that can facilitate the characterization of different systems at low cost and less complexity. Therefore, CFD represents a valuable complement of the experimental studies. However, there are little studies reporting the application of CFD modelling to absorbers in vapour absorption refrigeration systems [30–35]. A CFD model to assess a H_2O/LiBr membrane-based absorber was developed using the laminar model for the solution flow coupled to the multiphase model Mixture to solve the phase interactions [30]. Calculations were developed with a combination of the Semi-Implicit Method for Pressure Linked Equations, while the density and viscosity of the H_2O–LiBr were calculated with user define functions (UDF) as a function of the solution concentration and temperature. Results show that the solution film thickness mostly affects the mass transfer mechanism. The absorption rate increased by a factor of 3 when the solution channel thickness was reduced from 2 mm to 0.5 mm, while the absorption rate increased by a factor of 2.5 when the inlet solution flow velocity was increased from 0.00118 m s^{-1} to 0.00472 m s^{-1}. Moreover, a CFD model was developed to simulate the drop and jet flow regimes between the tubes in a falling film absorber using a solution of H_2O/LiBr [32]. The internal diameter of the tube was of 19.05 mm, while the space between tubes was of 24.5 mm. The thermophysical properties of the solution were considered constant in the range of the operating conditions assessed. The volume of fluid model (VOF) was used to represent the interface between the phases and an adaptative mesh refinement method was employed to increase the quality of the mesh and the accuracy of the mass diffusivity coefficient for water vapour in the aqueous LiBr solution. The results show that changing the regime from drops to jets, reduces the rate of average vapour mass flux one order of magnitude, from $6.3{\cdot}10^{-3}$ kg s^{-1} m^{-2} to $4.76{\cdot}10^{-4}$ kg s^{-1} m^{-2}. A CFD model was developed in a bubble absorber to evaluate the effect of two injectors with an injection angle of 30° to the vertical axis, on the heat and mass transfer processes using R134a-DMF [34]. The absorber consisted of a vertical tube with 65 mm of internal diameter and 5 mm of thickness. The methodology followed in this study includes the use of the k-ω SST model coupled with the multiphase model mixture to solve the phase interactions, while the user define function was employed for the solution thermophysical properties estimation. The results show that the heat and mass transfer coefficients increased 40% and 170%, respectively, contrasted to the no swirl case vertical nozzle. However, in this case, the mesh independent study and validation of the model are not clearly described. More recently, a CFD model was developed in Ansys-CFX to assess the performance of a flat plate absorber with NH_3/H_2O [35]. The absorber is a 3 channels plate heat exchanger, where the refrigerant vapour and solution flowed downward in the central channel while the cooling water flowed upward in the side channels. The geometry consisted in an absorber with eight gas injectors and 389 mm length, 127 mm depth, and

3.3 mm of thickness for the flow of the solution, 2.54 mm of thickness for the cooling flow. The k-ε turbulent model and the Navier Stokes equations were used in the CFD model to solve the heat and mass transfer processes. Results from the model were compared to the experimental from Kang et al. [36] in a plate absorber with offset strip fins and the data reported by Cerezo [37] in a plate absorber with internal corrugations. The model resulted in errors of 8.2% for the outlet cooling temperature, 4.2% for the outlet solution temperature, and 18.5% for the outlet ammonia mass fraction in the solution.

Although these studies demonstrated the potential of CFD methodologies to assess absorbers with working fluids such as NH_3/H_2O and H_2O/LiBr, various geometry configurations, and operating conditions, there are methodological gaps that need to be clarified. For example, it is unclear which criteria must be considered to adequately select the number of elements for the mesh, which variables are adequate for mesh independence test validation, and which methodology to follow for the model validation. In previous studies, the model validation has been based on the mean absolute error.

This study aims at assessing a tubular bubble absorber using $NH_3/LiNO_3$ by means of a CFD model, considering an adequate methodological process for validation. To this end, the development of a three-dimensional (3D) CFD absorber model is presented in detail, to characterize the heat and mass transfer processes using the $NH_3/LiNO_3$ solution. Data from 11 experimental tests is used to validate the model, using the absolute mean deviation (AMD%) and the relative mean deviation (RMD%) as measures of the error between the model results and the experimental data series. Additionally, the sum of squared errors (SSE), the root mean square error (RMSE), and root mean square deviation (RMSD) are considered in the validation.

2. Methodology for the absorber modelling

In this section is described the methodology followed for the development of the CFD model of the absorber under study.

2.1. Description of the absorber and test conditions

The bubble absorber considered is a vertical double pipe heat exchanger as shown in Fig. 1.

The cooling water flows downward through the annular channel, while the solution and vapour flow upward in the internal channel. The operating conditions considered for the CFD absorber model to simulate the absorption process, correspond to those of $NH_3/LiNO_3$ absorption chillers driven with low temperature heat sources, as considered for experimentation in Refs. [38,39].

The dimensions of the double pipe bubble absorber are shown in Table 1. The operating conditions of the absorber are presented in Table 2.

The mass fraction of ammonia in the solution at the absorber inlet was set to 0.45. The variables selected to assess the performance of the absorber with the CFD model are the solution temperature, ammonia mass fraction, absorption mass flux, and solution heat transfer coefficient at the absorber outlet. The absorption mass flux was estimated as in Ref. [38], whereas the solution heat transfer coefficient was obtained directly from the CFD model.

2.2. CFD model details

The 3D-CFD model was developed using the software ANSYS Fluent® (V.19.2), and a Dell Precision TX3500 workstation with an Intel®Xeon® X3470 processor (8 MB Cache, 2.93 GHz, Turbo, HT).

2.2.1. Geometry and mesh details

The 3D geometry of the tubular bubble absorber was built using ANSYS Design Modeler® software (ANSYS, Inc. V.19.2), using the finite volume method for discretization. Moreover, the computational domain was divided into 27,402 hexagonal elements and 83,576 nodes using the Ansys Inc® Meshing. The quality of mesh elements was evaluated using the orthogonal quality method with a

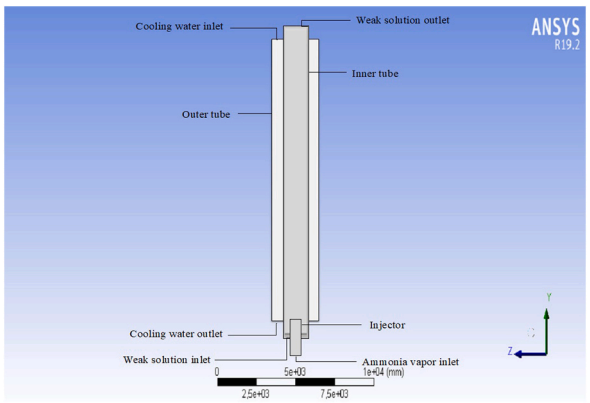

Fig. 1. Scheme of the bubble absorber implemented in the CFD.

Table 1
Dimension of the tubular absorber components.

Parameter	Outer tube (m)	Inner tube (m)	Injector (m)
External diameter	0.0150	0.0095	0.0037
Hydraulic diameter	0.0035	0.0075	0.0017
Length	1.0	1.1	0.008

Table 2
Operating conditions of the absorber for the CFD simulations.

Parameters	Mass Flow (kg h^{-1})	Inlet temperature (K)	Pressure (Pa)
Cooling water	91.05–109.5	308.2–313.8	$2.00 \cdot 10^5$
$NH_3/LiNO_3$ solution	20.2–71.5	318.15	$5.16 \cdot 10^5$
NH_3 vapour	0.01	298.15	$5.50 \cdot 10^5$

maximum value of 0.99966 (SD 0.23873) and then skewness method with a maximum value of 0.97424 (SD 0.2087). In both cases, the best quality of the elements coincides when values are close to 1.0. This procedure was implemented to improve both the solution accuracy and the model convergence. Fig. 2 and Fig. 3 depict the geometry and mesh of the 3D-CFD model developed.

Four mesh densities with different cell sizes were used in the CFD model:

- Mesh 1: 27,402 elements with 83,576 nodes,
- Mesh 2: 87,326 elements producing 261,978 nodes,
- Mesh 3: 128,877 elements producing 230,791 nodes,
- Mesh 4: 554,804 elements producing 846,193 nodes.

The mesh independence test is an essential step to develop a CFD model, which guarantees the quantity of the mesh elements and that results are not meshing dependent. Therefore, an adequate study selecting the variables to assess the performance of the mesh is required. The mesh independence test discussed in Ref. [35], uses the mass fraction of ammonia and the temperature profiles of the solution as variables for the mesh independence test. The model was validated using the outlet ammonia concentration (with an error of 18.5%) and the outlet solution temperature (with an error of 4.2 %) using a mesh of 48,000 elements. In a different study, Asfand et al. [30] selected the ammonia absorption rate as the variable for the mesh independence test. The results of the model using a mesh size of 15 × 15,000 cells, were compared to one set of experimental data, pointing to errors lower than 1 % in the absorption rate. However, the methodology used is not described in the study and it is unclear how these results were obtained.

In this study, the test of the model grid independence was initially conducted using the solution temperature profiles and the ammonia concentration at the outlet of the inner tube. These results are presented in sub-section 3.2.

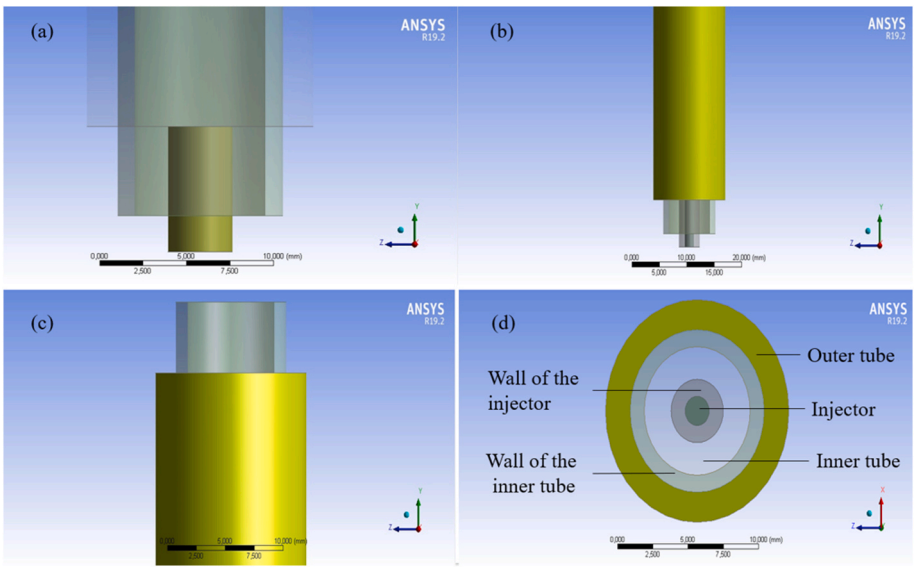

Fig. 2. Geometry of the CFD model, (a, b, c) lateral views, and (d) top view.

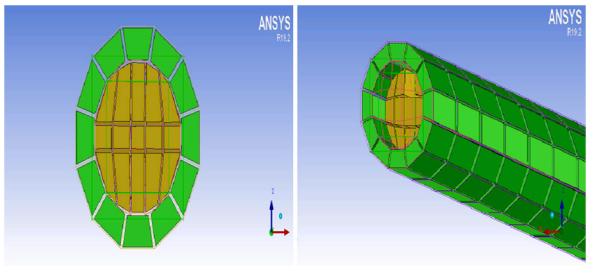

Fig. 3. Mesh used in the discretization of the CFD model.

2.2.2. Multiphase models selection

Three multiphase models were tested in the CFD model:

- Volume of fluid (VOF).
- Mixture.
- Eulerian.

Furthermore, four Eulerian Phases from the material panel were used in the 3D-CFD model:

- Phase 1: ammonia-lithium nitrate solution.
- Phase 2: ammonia vapour.
- Phase 3: water liquid.
- Phase 4: ammonia liquid.

Additionally, two mass transfer mechanism were activated from phase 2 to phase 1 and from phase 2 to phase 4 with constant rate (1/s). Moreover, seven viscous models were tested in the CFD model:

- Laminar model.
- The k-epsilon models series (standard, RNG and realizable).
- The k-omega models series (standard, BSL and SST).

Best results in terms of the residual convergence (10^{-7}) were obtained with the Realizable k-epsilon model. Therefore, this model was selected for the 3D-CFD model. Finally, the energy equation was activated to simulate the heat transfer process and the temperature profiles in the absorber.

2.3. Governing equations

The governing equations are based on the Navier-Stokes equation solved for transient conditions in each phase. The three-dimensional continuity, momentum, turbulence, and energy equations, which were addressed using the Eulerian multiphase approach, are shown following:

Continuity equation

$$\frac{\partial}{\partial t}\left(\alpha_q \delta_q\right) + \nabla\left(\alpha_q \delta_q \vec{\vec{V}}_q\right) = \sum_{p=1}^{n}\left(\dot{m}_{pq} - \dot{m}_{qp}\right) + S_q \tag{1}$$

Equation for momentum

$$\frac{\partial}{\partial t} = (\rho\vec{v}) + \nabla.(\rho\vec{v}\vec{v}) = -\nabla_p + \nabla.(\bar{\bar{\tau}}) + \rho\vec{g} + \vec{F} \tag{2}$$

Turbulence model.

The $k-\varepsilon$ Realizable turbulence model equations are as follows:

$$\frac{\partial}{\partial t}(\rho k) + \frac{\partial}{\partial x_j}\left(k u_j\right) = \frac{\partial}{\partial x_j}\left[\left(\mu + \frac{\mu_t}{\sigma_k}\right)\frac{\partial k}{\partial x_j}\right] + G_k + G_b - \rho\varepsilon - Y_M + S_k \tag{3}$$

and,

$$\frac{\partial}{\partial t}(\rho\varepsilon) + \frac{\partial}{\partial x_j}\left(\rho\varepsilon u_j\right) = \frac{\partial}{\partial x_j}\left[\left(\mu + \frac{\mu_t}{\sigma_\varepsilon}\right)\frac{\partial \varepsilon}{\partial x_j}\right] + \rho C_1 S\varepsilon - \rho C_2 \frac{\varepsilon^2}{k + \sqrt{\nu\varepsilon}} + C_{1\varepsilon}\frac{\varepsilon}{k}C_{3\varepsilon}G_b + S_\varepsilon \tag{4}$$

The following default turbulence coefficients in the model were used: $C_1 = 1.44$, $C_2 = 1.92$ and $C_3 = 0.09$.
Conservation of energy was described using the following equation:
Energy equation

$$\frac{\partial}{\partial t}(\rho E) + \nabla.(\vec{v}\,(\rho E + p)) = \nabla.\left(k_{eff}\nabla T - \sum_{j}^{n} h_j \vec{J}_j + \left(\bar{\bar{\tau}}_{eff}.\vec{v}\right)\right) + S_h \tag{5}$$

More details on the formulated equations can be found in Refs. [40,41].

2.4. Boundary conditions and solution methods

The boundary conditions used in the CFD model are show in Table 3. At the inlet, the boundary condition "pressure inlet" establishes the fluid pressure for the inlet flow. It is suitable for both, incompressible and compressible flow calculations. The "pressure outlet" boundary condition was used in the outlets, because it was compatible with the multiphase model selected [40]. The boundary "wall" was applied to the walls to simulate the solid boundary conditions of the bubble absorber. Walls in the CFD model were treated as stationary, and the shear condition selected for walls was the "no-slip".

The solution methods used include a solver type that is pressure-based coupling with velocity formulation absolute in transient state. The absolute velocity formulation is recommended for low velocities in the flow [40]. The time step considered in the simulations was of 0.001 (s), with a minimum number of time steps of 2200 required for a good performance of the model. Table 4 shows the solution methods selected.

Finally, the thermophysical properties of the liquid water, ammonia vapour, and ammonia liquid were determined from the Fluent software data base. The water was assumed to be incompressible, exhibiting Newtonian behaviour, while material properties were considered constant during the simulations. The thermodynamic properties for the $NH_3/LiNO_3$ solution were obtained from Refs. [42–44], while the enthalpy values were estimated according to the methodologies reported in Refs. [45,46].

2.5. Conditions for CFD model validation

To validate the CFD model, its results were compared to the experimental data reported in Ref. [38], which corresponds to the results obtained for a $NH_3/LiNO_3$ tubular bubble absorber with smooth surfaces. First, the normality of the simulated and experimental data series was validated using the Shapiro Wilks test ($n > 50$), where a $P > 0.05$ indicates normality. Additionally, the T-student test was used to compare the mean, the Mann-Whitney test was used to compare the ranges, and the Levene test was used to compare variances ($n > 50$). In this case, a $P > 0.05$ indicates that there are not statistically significant differences between the data series.

The accuracy tests were used to compare the simulated results for temperature, ammonia concentration, absorption mass flux, and solution heat transfer coefficient with the experimental data. Accuracy tests include the calculation of the absolute mean deviation (AMD%), and the relative mean deviation (RMD%) as measures of the error between the simulated and experimental data series. Additionally, the sum of the squared estimate errors (SSE), the root mean square error (RMSE) and the root mean square deviation (RMSD).

3. Results and discussion

This section provides the results obtained from the calibration and validation of the CFD model. It also shows the capability of the CFD model to predict the performance of the absorber at different solution mass flows and cooling water temperatures.

Table 3
Boundary conditions of the CFD model.

Zone	Boundary	Observations
Annulus inlet side	Pressure inlet; direction specification method: normal to boundary	$I = 0.185\%$, $k = 0.1006\ m^2\ s^{-2}$, $\varepsilon = 0.172\ m^2\ s^{-3}$, volume fraction for phase 3 (water): 1.0
Inner tube inlet		$I = 0.316\%$, $k = 2.53 \cdot 10^{-3}\ m^2\ s^{-2}$, $\varepsilon = 4.03 \cdot 10^{-4}\ m^2\ s^{-3}$, NH_3 mass fraction for phase 4 ($NH_3/LiNO_3$ solution): 0.452
Injector inlet		$I = 0.567\%$, $k = 7.17 \cdot 10^{-5}\ m^2\ s^{-2}$, $\varepsilon = 1.07 \cdot 10^{-6}\ m^2\ s^{-3}$, volume fraction for phase 2 (ammonia vapour): 1.0
Annulus outlet side	Pressure oulet; backflow direction specification method: normal to boundary	$k = 0.01\ m^2\ s^{-2}$, $\varepsilon = 0.01\ m^2\ s^{-3}$ Pressure $= 2.0 \cdot 10^5$ Pa
Inner tube outlet		$k = 0.01\ m^2\ s^{-2}$, $\varepsilon = 0.01\ m^2\ s^{-3}$ Pressure $= 5.13 \cdot 10^5$ Pa
Injector outlet	Contact region-interface	Pressure $= 5.13 \cdot 10^5$ Pa
Walls	Stationary Wall	Steel

*I: turbulence intensity; k and ε: parameters of the turbulence model.

Table 4
Solution methods selected.

Variable	Methods
Scheme	PISO
Gradient	Least squares cell based
Pressure	Presto
Momentum	Third-Order-MUSCL
Volume fraction	Compressive
Energy	Third-Order-MUSCL
Turbulent kinetic energy	Third -Order-MUSCL
Turbulent dissipation rate	Third -Order-MUSCL
Transient formulation	Second order implicit

3.1. Calibration and validation of the CFD model

3.1.1. Turbulence and mixture models selection

The Volume of Fluid model (VOF) [30,32] and the Mixture model [34] have been used in other studies, and were tested in the initial simulations under steady-state conditions. The initial tests were conducted at a solution mass flow of 20 kg h^{-1}, inlet solution temperature of 318.7 K, ammonia concentration of 0.4587, cooling water temperature of 101.3 kg h^{-1} and cooling water temperature of 311.54 K.

Table 5 shows that in terms of the solution convergence, the VOF model shows the best model with 25% less computational time, and a lower magnitude of residuals (10^{-7}), with an explicit formulation and interface modelling sharp/dispersed. In agreement with [40], it was designed for two or more immiscible fluids where the position of the interface between the fluids is of interest. In this model, the fluids shared a single set of momentum equations, tracking the volume fraction of each fluid in each computational cell throughout the domain.

Moreover, for the viscous model, the best results were obtained with the Realizable k-epsilon model coupled with the VOF model, for different validations of separated flows and flows with complex secondary features like it is the case in bubble absorbers.

3.1.2. Mesh independence test

The present study considers the solution temperature (T) and ammonia concentration (X_{NH3}) at the outlet of the absorber for the mesh independence test. Table 6 shows the mesh independence test for the present study contrasted to experimental data for a solution temperature of 320.95 K and ammonia concentration of 0.4587.

Table 6 shows that the errors for the outlet solution temperature and ammonia concentration in the four mesh densities are below 3.5% which represents a good mesh performance in all the cases. Also, it can be noted that the mesh 2 reduced the error in 17% and 10% respectively, contrasted to mesh 1. However, the computational time increased by 44%. Moreover, contrasted to mesh 1, mesh 3 reduced the error in 50% and 94% respectively, while the computational time increased by 156%. Finally, mesh 4 reduces the error in 67% and 48% respectively, while the computational time increased by 367 %. These results show that the computational time increases linearly with the mesh size, while the error reduces at a lower rate, and can even increase like the error for X_{NH3} in mesh 4.

Based on these results, the mesh quality criteria implemented, and considering that errors are low enough for all the cases, mesh 1 stand as an adequate alternative for the CFD simulations.

3.1.3. Mass transfer results

The CFD model developed permitted to obtain the outlet ammonia concentration and the absorption mass flux in the inner tube of the absorber at different operating conditions according to Table 2. Fig. 4 shows the comparison between predicted and experimental data for the outlet ammonia concentration. Results show that at the given operating conditions and considering mesh 1, the error between predicted and experimental data for the outlet ammonia concentration is in the range of ±0.7%. The predicted values evidence a clear trend and an adequate slope. Results indicate that apparently, the mesh 1 could be used to evaluate the absorber performance using the CFD model. However, Fig. 5 shows that errors for the ammonia absorption mass flux are significantly higher in the range of ±40%., with disperse results that show no clear trend. These results can be explained because of the low quantity of mesh elements used near to the walls of the tubes and vapour-liquid interphase.

Based on the high errors in the ammonia absorption mass flux, mesh 2 with 128,877 elements was used to test its effect on the absorption mass flux prediction. Fig. 5 shows that a mesh with more elements improves the ammonia absorption mass flux prediction.

Table 5
Results of the multiphase models used.

Parameters	VOF model	Mixture Model	Eulerian Model
Solution	Converged	No converged	Diverged
Residuals	10^{-7}	10^{-3}	Diverged
Computational time (h)	4.5	6	6
Memory requirements (GB)	5	11	11

Table 6
Predicted temperature and ammonia concentration profiles for each mesh assessed for the CFD model.

Mesh	Elements	CFD-model		Error (%)		Computational time (h)	Memory requirement (GB)
		T (K)	X_{NH3} (w/w)	T	X_{NH3}		
1	27,402	317.2	0.4734	1.2	3.1	1.8	0.5
2	87,326	317.6	0.4719	1.0	2.8	2.6	0.5
3	128,877	318.5	0.4532	0.6	0.2	4.6	1.0
4	554,804	319.6	0.4662	0.4	1.6	8.4	1.2

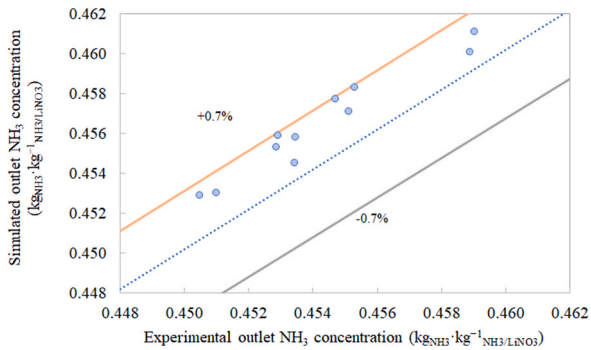

Fig. 4. CFD model results with mesh 1 vs. experimental results [38] for the outlet ammonia concentration.

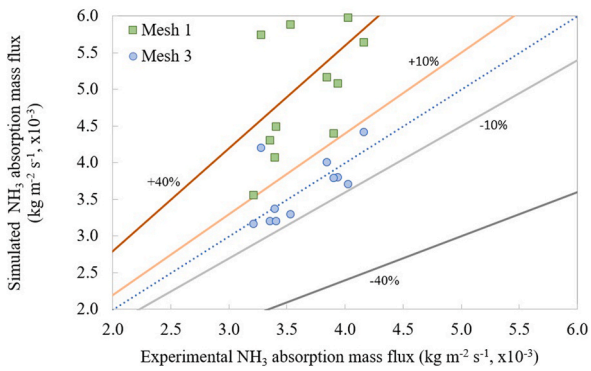

Fig. 5. CFD model results with mesh 1 and mesh 3 vs. experimental results [38] for the absorption mass flux.

Results are now within an error of ±10% with a mean error of 6.6% while the trend of the results is well defined.

These results evidence that, regardless of the low error of the outlet ammonia concentration of the CFD model, the mesh independence test must also include the ammonia absorption mass flux. Furthermore, the validation of the CFD model must be developed

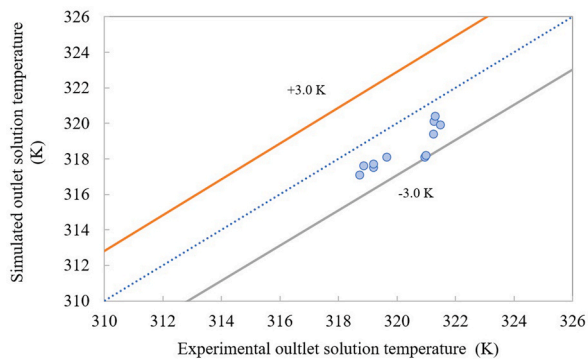

Fig. 6. CFD model results vs. experimental results for the outlet solution temperature.

using sufficient experimental data to test the performance of the CFD model in different points, and adequately predict the effect of different variables on the absorption process.

3.1.4. Heat transfer results

The results of the CFD model for the outlet solution temperature and solution heat transfer coefficient were contrasted to the experimental data in Ref. [38] and presented as follows. The results presented were obtained using mesh 2. Fig. 6 shows the solution temperature at the centre of the outlet of the inner tube for mesh 3.

The results show a temperature deviation under ±3 K as compared to the experimental data, which correspond to errors lower than 1%. In fact, 82% of the simulation data presented temperature deviations lower than ±1.8 K. The highest accuracy on the results were obtained for inlet solution flow rates over 30 kg h^{-1}. Results between 318 K and 320 K correspond to a cooling water temperature of 308.15 K, while results between 320 K and 322 K correspond to a cooling water temperature of 313.15 K. The values predicted with the model for the solution temperature, evidence that the model can adequately simulate the heat transfer process between the solution side and the cooling water side. This demonstrates the robustness of the CFD model to simulate the effect of this variable.

Moreover, the comparison between the results of the CFD model and the experimental data for the solution heat transfer coefficient is presented in Fig. 7. It is important to highlight that the LMTD for the experimental solution heat transfer coefficient was obtained considering equilibrium conditions for the outlet solution flow. Results can be different depending on how the LMTD is approached. The results show error values lower than ±7%, where the error is lower than ±5% for 82% of the data and the mean error is around 3.3%, showing a clear trend and correspondence between the CFD model results and the experimental data.

3.1.5. Model validation

One issue of CFD methodologies discussed in literature is related to the model validation based on the CFD model results. In some studies, there is either no report of a validation process included, or the validation is conducted using a single set of experimental data, using variables like temperature, ammonia concentration, or ammonia absorbed. In this study, a validation methodology is describe to increase the reliability of the results. In this case, the validation includes the statistical comparison of the variables reported in the specialized literature: outlet temperature solution, outlet ammonia concentration, solution heat transfer coefficient, and absorption mass flux.

The Shapiro-Wilks test showed that only the data series of ammonia concentration corresponded to a normal distribution, therefore, the T-student test was used to compare the mean Mann-Whitney test and compare the ranges, whereas the Levene test was used to compare variances. According to Table 7, results show that there are no statistical differences between the experimental and simulated data series of ammonia concentration and solution temperature at the outlet of the inner tube ($P > 0.05$), supporting the percentages of error obtained in the previous sections. Conversely, the experimental and simulated data series for absorption mass flux and solution heat transfer coefficient do not present statistical differences for the indicators compared ($P < 0.05$). This means that the CFD model with 128,877 mesh elements (i.e. mesh 2), provides adequate accurate results for the four evaluated variables considered in the validation. The deviations in the accuracy tests varied from 1% to 11%, which confirms the statistical results and accuracy of the CFD model contrasted to the experimental data series. It demonstrates that the 3D-CFD model implemented is robust and have good accuracy and precision.

3.2. Solution flow and cooling water temperature vs absorber performance

This sub-section shows the effect of the solution mass flow and cooling water temperature on the absorption mass flux, solution heat transfer coefficient, and solution temperature profile.

Fig. 8 shows the ammonia absorption mass flux of the CFD model as a function of the solution mass flow and cooling water temperature (Tcw). Results indicate that at the given solution mass flows, the absorption mass flux varies between 0.00316 kg m^{-2} s^{-1} and 0.00420 kg m^{-2} s^{-1} for a cooling water temperature of 313.15 K, whereas it varies between 0.00370 kg m^{-2} s^{-1} and 0.00441 kg m^{-2} s^{-1} for a cooling water temperature of 308.15 K. As discussed in Ref. [39], the mass flow set for the flow of cooling water (corresponding to the transition regime) limits the potential of the absorption mass flux when increasing the solution mass flux for each cooling water temperatures. That is the reason why at the given conditions, the absorption mass flux does not tend increase for solution mass flows between 20 kg h^{-1} and 60 kg h^{-1}. Moreover, the results from the CFD model show that small increments in the absorption mass flux are obtained at the highest mass flow set for each cooling water temperature. Also, the CFD model adequately interpretate the effect of the cooling water temperature on the absorption mass flux that increases as the cooling water temperature decreases. This effect is explained because of the higher potential for absorption when improving the heat dissipation of the exothermic heat generated during this process.

Fig. 9 depicts the solution heat transfer coefficient in the CFD model as a function of the solution mass flow and cooling water temperature. Results indicate that for defined solution mass flows, the solution heat transfer coefficient ranges between 490 W m^{-2} K^{-1} and 709 W m^{-2} K^{-1} for a cooling water temperature of 313.15 K. Moreover, for a cooling water temperature of 308.15 K, the solution heat transfer coefficient ranges between 457 W m^{-2} K^{-1} and 786 W m^{-2} K^{-1}. As expected, the solution heat transfer coefficient rises when the solution mass flow is increased, and the cooling water temperature is reduced. This trend is evident since, increasing the solution mass flow and reducing the cooling water temperature, result in a rise of the heat transfer rate higher than the rise of logarithmic mean temperature difference (LMTD).

Fig. 10 shows the temperature profile in the inner tube at 0.1 m intervals. The temperature profiles taken in the tube centre show that between 0.1 m and 0.8 m, the temperature increases at a rate of 0.64 K–1.07 K, while between 0.8 and 1 m the increasing rate is

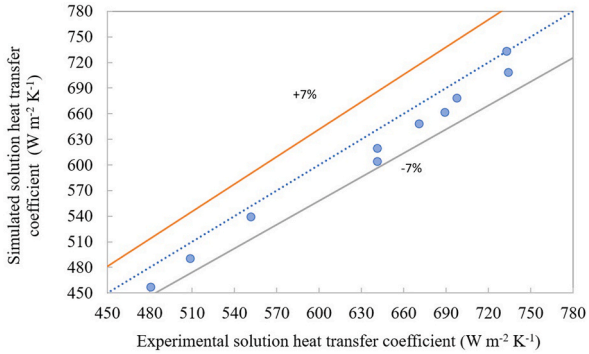

Fig. 7. CFD model results vs. experimental results for the solution heat transfer coefficient.

Table 7
Results of the accuracy test.

Test	Exp.	Sim.	Exp.	Sim.	Exp.	Sim.	Exp.	Sim.
	Outlet mass fraction (kg_{NH3} $kg^{-1}_{NH3/LiNO3}$)		Outlet solution temperature (K)		Absorption mass flux kg $m^{-2}s^{-1}$		Solution heat transfer coefficient W $m^{-2}K^{-1}$	
AMD	0.0021	0.0018	1.031	0.920	0.0003	0.0003	77.95	79.59
RMD	0.61	0.50	0.34	0.29	9.28	11.95	15.45	16.13
SSE	0.00006	0.00003	11.62908	12.56397	0.00000	0.00000	101,065	103,100
RMSE	0.00001	0.00000	1.05719	1.24000	0.00000	0.00000	9188	9373
RMS	0.45430	0.45322	320.093	318.449	0.00366	0.00367	658	634

*Exp. – Experimental, Sim. – Simulated; AMD – Absolute mean deviation; RMD – Relative mean deviation; SSE – Sum of the squared errors; RMSE – Root mean square error; RMS – Root mean square deviation.

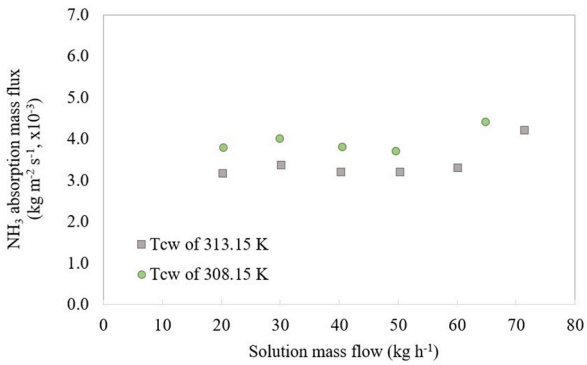

Fig. 8. Simulated absorption mass flux vs. solution mass flow for two cooling water temperatures.

significantly lower ranging from 0.2 K to 0.4 K. This indicates the heat and mass transfer rates in the final section are lower than those at the initial section, suggesting that the solution is close to its equilibrium conditions. Considering that the inlet solution temperature was set to 318.15 K while the vapour inlet temperature was set to 298.15 K, it is observed that in the first absorber section centre, up to 0.1 m, the temperature is lower than the inlet solution temperature. Then, the temperature increases progressively along the absorber length because of the exothermic absorption process. Moreover, when the temperature is measured in a medium point between the tube centre and the inner tube internal surface, the temperature profile changes drastically indicating that different temperature gradients can be found in the radial axe with respect to the centre along the absorber length. This means that the temperature in the tube centre is affected by the inlet ammonia flow temperature while the ammonia is absorbed by the solution flow and the saturation condition is reached.

Fig. 10 also shows that the solution temperature measured at the outlet of the absorber can vary depending on the measurement point. At the medium point between the tube centre and the inner tube internal surface, the solution outlet temperature is higher than that at the tube centre. Considering that the outlet temperature values predicted by the model were underestimated (see Fig. 6), outlet solution temperature measurements at the medium point mentioned before are closer to the experimental values.

Furthermore, results also show that the outlet solution temperature increases with increasing the solution mass flow, because of the higher absorption rate. Moreover, at the same solution flow, the outlet solution temperature decreases for lower cooling water

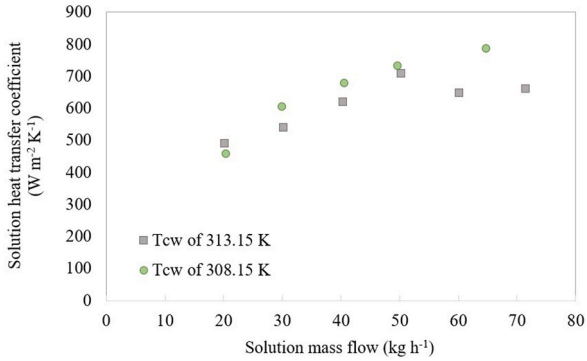

Fig. 9. Simulated solution heat transfer coefficient vs. solution mass flow and cooling water temperature.

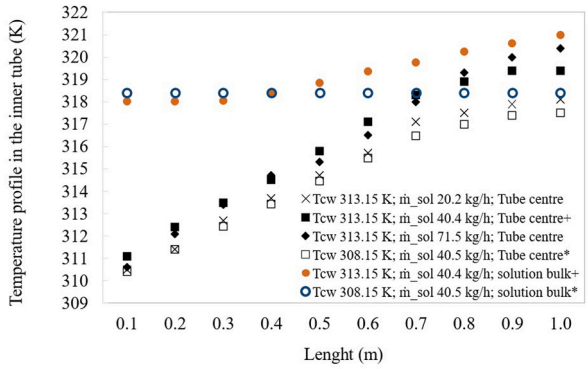

Fig. 10. Solution temperature profile in the inner tube.

temperatures, because it improves the heat transfer potential between the solution and cooling water flow.

4. Conclusions

In this study, a CFD bubble absorber model was developed and used to simulate the absorption process in a tubular absorber using the $NH_3/LiNO_3$ solution. Results reported were compared against experimental data from the literature whereas a proper validation of the model was also reported. The following conclusions can be drawn from this study:

- The Volume of Fluid model coupled with the Realizable k-epsilon model are adequate to simulate the simultaneous heat and mass transfer processes in a $NH_3/LiNO_3$ tubular absorber considering the lowest residuals, computational time, and memory requirements.
- The mesh independence test showed that the outlet temperature and mass fractions are not reliably parameters for this study. Even when low errors are obtained for these variables, the solution heat transfer coefficient and absorption mass flux can present high errors. Therefore, an appropriate methodology for the mesh independence test should include these heat and mass transfer variables.
- Results indicated that further mesh refinement can be required to improve the CFD model accuracy when considering parameters like the absorption mass flux and solution heat transfer coefficient. Results in this study showed that the validation of the model is essential to guarantee adequate results from the CFD model. All in all, the validation results showed that there are no significant statistical differences between experimental and simulated data series.
- The CFD model is reliable to simulate the absorption process in a $NH_3/LiNO_3$ vertical double pipe heat exchanger bubble absorber considering the effect of the solution mass flow and cooling water temperature. In this case, the absorption mass flux obtained ranged between 0.00316 kg m^{-2} s^{-1} and 0.00420 kg m^{-2} s^{-1} and between 0.00370 kg m^{-2} s^{-1} and 0.00441 kg m^{-2} s^{-1} for a cooling water temperature of 313.15 K and 308.15 K. Meanwhile, the solution heat transfer coefficient ranged between 490 W m^{-2} K^{-1} and 709 W m^{-2} K^{-1}, and between 457 W m^{-2} K^{-1} and 786 W m^{-2} K^{-1} for the corresponding cooling water temperatures.
- The temperature profiles in the solution side of the absorber showed temperature gradients in the radial axe with respect to the tube centre along the absorber length, due to the temperature difference between the inlet solution flow and the inlet ammonia flow. These temperature gradients could not be identified in experimental studies or from simulations using one-dimensional models.

- The CFD model developed will be used to study heat and mass transfer enhancement techniques, developing advanced bubble absorber designs, and exploring new working fluids.

CRediT authorship contribution statement

Andrés Zapata: Methodology, Investigation, Formal analysis, Validation, Writing – original draft, Visualization, Software, Funding acquisition. **Carlos Amaris:** Conceptualization, Methodology, Investigation, Formal analysis, Validation, Writing – original draft, Writing – review & editing. **Alexis Sagastume Gutiérrez**: Investigation, Formal analysis, Writing – review & editing. **Andrés Rodríguez:** Investigation, Funding acquisition, Writing – review & editing.

Declaration of competing interest

The authors declare that they have no known competing financial interests or personal relationships that could have appeared to influence the work reported in this paper.

Acknowledgments

Andres Zapata thanks to the Universidad de la Costa and Minciencias for the postdoctoral grant #848 and for the financial support provided during this research project. This study is part of the research project CONV-13-2018 and CONV-15-2020 funded by the Universidad de la Costa and Minciencias.

References

[1] G.A. Florides, S.A. Tassou, S.A. Kalogirou, L.C. Wrobel, Review of solar and low energy cooling technologies for buildings, Renew. Sustain. Energy Rev. 6 (2002) 557–572.
[2] J. Mendoza, J. Rhenals, A. Avila, A. Martinez, T. De la Vega, E. Durango, Heat absorption cooling with renewable energies: a case study with photovoltaic solar energy and biogas in Cordoba, Colombia, INGE CUC 17 (2021) 1–10, https://doi.org/10.17981/ingecuc.17.2.2021.01.
[3] K.R. Ullah, R. Saidur, H.W. Ping, R.K. Akikur, N.H. Shuvo, A review of solar thermal refrigeration and cooling methods, Renew. Sustain. Energy Rev. 24 (2013) 499–513, https://doi.org/10.1016/J.RSER.2013.03.024.
[4] C. Amaris, B.C. Miranda, M. Balbis-Morejón, Experimental thermal performance and modelling of a waste heat recovery unit in an energy cogeneration system, Therm. Sci. Eng. Prog. 20 (2020), https://doi.org/10.1016/j.tsep.2020.100684.
[5] Y.T. Ge, S.A. Tassou, I. Chaer, N. Suguartha, Performance evaluation of a tri-generation system with simulation and experiment, Appl. Energy 86 (2009) 2317–2326, https://doi.org/10.1016/j.apenergy.2009.03.018.
[6] D.S. Ayou, J.C. Bruno, R. Saravanan, A. Coronas, An overview of combined absorption power and cooling cycles, Renew. Sustain. Energy Rev. 21 (2013) 728–748, https://doi.org/10.1016/j.rser.2012.12.068.
[7] M. Mittermaier, F. Ziegler, Theoretical evaluation of absorption and desorption processes under typical conditions for chillers and heat transformers, Int. J. Refrig. 59 (2015) 91–101, https://doi.org/10.1016/j.ijrefrig.2015.07.015.
[8] P. Srikhirin, S. Aphornratana, S. Chungpaibulpatana, A review of absorption refrigeration technologies, Renew. Sustain. Energy Rev. 5 (2000) 343–372, https://doi.org/10.1016/S1364-0321(01)00003-X.
[9] C. Amaris, M. Bourouis, Boiling process assessment for absorption heat pumps: a review, Int. J. Heat Mass Tran. 179 (2021) 121723, https://doi.org/10.1016/J.IJHEATMASSTRANSFER.2021.121723.
[10] C. Amaris, M. Vallès, M. Bourouis, Vapour absorption enhancement using passive techniques for absorption cooling/heating technologies: a review, Appl. Energy 231 (2018) 826–853, https://doi.org/10.1016/j.apenergy.2018.09.071.
[11] Y.T. Kang, A. Akisawa, T. Kashiwagi, Analytical investigation of two different absorption modes: falling film and bubble types, Int. J. Refrig. 23 (2000) 430–443.
[12] X. Wu, S. Xu, M. Jiang, Development of bubble absorption refrigeration technology: a review, Renew. Sustain. Energy Rev. 82 (2018) 3468–3482, https://doi.org/10.1016/J.RSER.2017.10.109.
[13] M.A. Johnson, J. De La Peña, R.B. Mesler, Bubble shapes in nucleate boiling, AIChE J. 12 (1966) 344–348, https://doi.org/10.1002/aic.690120225.
[14] Y.T. Kang, T. Nagano, T. Kashiwagi, Visualization of bubble behavior and bubble diameter correlation for NH 3 ± H 2 O bubble absorption Â lation entre le comportement de la bulle et Etude de la corre Á tre lors d ' absorption NH 3 -H 2 O : de son diame Â thode visuelle me, Int. J. Refrig. 25 (2002) 127–135.
[15] T.L. Merrill, H. Perez-Blanco, Combined heat and mass transfer during bubble absorption in binary solutions, Int. J. Heat Mass Tran. 40 (1997) 589–603, https://doi.org/10.1016/0017-9310(96)00118-4.
[16] K. Terasaka, J. Oka, H. Tsuge, Ammonia absorption from a bubble expanding at a submerged orifice into water, Chem. Eng. Sci. 57 (2002) 3757–3765, https://doi.org/10.1016/S0009-2509(02)00308-1.
[17] T. Elperin, A. Fominykh, Four stages of the simultaneous mass and heat transfer during bubble formation and rise in a bubbly absorber, Chem. Eng. Sci. 58 (2003) 3555–3564, https://doi.org/10.1016/S0009-2509(03)00192-1.
[18] M.D. Staicovici, A non-equilibrium phenomenological theory of the mass and heat transfer in physical and chemical interactions: Part II — modeling of the NH3/H2O bubble absorption, analytical study of absorption and experiments, Int. J. Heat Mass Tran. 43 (2000) 4175–4188, https://doi.org/10.1016/S0017-9310(00)00030-2.
[19] M.D. Staicovici, A non-equilibrium phenomenological theory of the mass and heat transfer in physical and chemical interactions: Part I — application to NH3/H2O and other working systems, Int. J. Heat Mass Tran. 43 (2000) 4153–4173, https://doi.org/10.1016/S0017-9310(00)00029-6.
[20] M. Suresh, A. Mani, Heat and mass transfer studies on R134a bubble absorber in R134a/DMF solution based on phenomenological theory, Int. J. Heat Mass Tran. 53 (2010) 2813–2825, https://doi.org/10.1016/j.ijheatmasstransfer.2010.02.016.
[21] M.K. Aggarwal, R.S. Agarwal, Thermodynamic properties of lithium nitrate-ammonia mixtures, Int. J. Energy Res. 10 (1986) 59–68, https://doi.org/10.1002/er.4440100107.
[22] A.A.S. Lima, A.A.V. Ochoa, J.Â.P. Da Costa, F. dos Santos, A.C. Carlos, Lima, V.F. Márcio, de Menezes, Energetic analysis of an absorption chiller using NH3/LiNO3 as an alternative working fluid, Braz. J. Chem. Eng. 36 (2019) 1061–1073, https://doi.org/10.1590/0104-6632.20190362s20180473.
[23] J.M. Abdulateef, K. Sopian, M.A. Alghoul, Optimum design for solar absorption refrigeration systems and comparison of the performances using ammonia-water, ammonia-lithium nitrate and ammonia-sodium thiocyanate solutions, Int. J. Mech. Mater. Eng. 3 (2008) 17–24.
[24] R. Ayala, J.L. Frías, L. Lam, C.L. Heard, F.A. Holland, Experimental assessment of an ammonia/lithium nitrate absorption cooler operated on low temperature geothermal energy, Heat Recovery Syst. CHP 14 (1994) 437–446, https://doi.org/10.1016/0890-4332(94)90047-7.
[25] C. Amaris, M. Bourouis, M. Vallès, Passive intensification of the ammonia absorption process with NH3/LiNO3 using carbon nanotubes and advanced surfaces in a tubular bubble absorber, Energy 68 (2014) 519–528, https://doi.org/10.1016/j.energy.2014.02.039.

[26] A.A.S. Lima, G.N.P. Leite, A.A.V. Ochoa, C.A.C. Dos Santos, J.A.P. da Costa, P.S.A. Michima, A.M.A. Caldas, Absorption refrigeration systems based on ammonia as refrigerant using different absorbents: review and applications, Energies 14 (2021), https://doi.org/10.3390/en14010048.
[27] C.A. Infante Ferreira, Combined momentum, heat and mass transfer in vertical slug flow absorbers, Int. J. Refrig. 8 (1985) 326–334.
[28] J. Cerezo, R. Best, R.J. Romero, A study of a bubble absorber using a plate heat exchanger with NH_3-H_2O, NH_3-$LiNO_3$and NH_3-NaSCN, Appl. Therm. Eng. 31 (2011) 1869–1876, https://doi.org/10.1016/j.applthermaleng.2011.02.032.
[29] C. Amaris, M.E. Alvarez, M. Vallès, M. Bourouis, Performance assessment of an NH3/LiNO3 bubble plate absorber applying a semi-empirical model and artificial neural networks, Energies 13 (2020), https://doi.org/10.3390/en13174313.
[30] F. Asfand, Y. Stiriba, M. Bourouis, CFD simulation to investigate heat and mass transfer processes in a membrane-based absorber for water-LiBr absorption cooling systems, Energy. https://doi.org/10.1016/j.energy.2015.08.018, 2015.
[31] F. Asfand, Y. Stiriba, M. Bourouis, Performance evaluation of membrane-based absorbers employing H2O/(LiBr + LiI + LiNO3 + LiCl) and H2O/(LiNO3 + KNO3 + NaNO3) as working pairs in absorption cooling systems, Energy. https://doi.org/10.1016/j.energy.2016.08.103, 2016.
[32] S.M. Hosseinnia, M. Naghashzadegan, R. Kouhikamali, CFD simulation of adiabatic water vapor absorption in large drops of water-LiBr solution, Appl. Therm. Eng. 102 (2016) 17–29, https://doi.org/10.1016/j.applthermaleng.2016.03.144.
[33] S.M. Hosseinnia, M. Naghashzadegan, R. Kouhikamali, CFD simulation of water vapor absorption in laminar falling film solution of water-LiBr — Drop and jet modes, Appl. Therm. Eng. 115 (2017) 860–873, https://doi.org/10.1016/j.applthermaleng.2017.01.022.
[34] S.K. Panda, A. Mani, CFD heat and mass transfer studies in a R134a-DMF bubble absorber with swirl flow entry of R134a vapour, Int. Compress. Eng. Refrig. Air Cond. High Perform. Build. Conf. (2016) 1–10.
[35] A.A.S. Lima, A.A. V Ochoa, J.A.P. Da Costa, J.R. Henríquez, CFD simulation of heat and mass transfer in an absorber that uses the pair ammonia/water as a working fluid, Int. J. Refrig. 98 (2019) 514–525, https://doi.org/10.1016/j.ijrefrig.2018.11.010.
[36] Y.T. Kang, T. Kashiwagi, R.N. Christensen, Ammonia-water bubble absorber with a plate heat exchanger, ASHRAE Trans., 1998, pp. 1565–1575.
[37] J. Cerezo, Estudio del proceso de absorción con amoníaco-agua en intercambiadores de placas para equipos de refrigeración por absorción, Universitat Rovira i Virgili, 2006.
[38] C. Amaris, Intensification of NH3 Bubble Absorption Process Using Advanced Surfaces and Carbon Nanotubes for NH3/LiNO3 Absorption Chillers, Universitat Rovira i Virgili, Tarragona, Spain, 2013. https://www.tdx.cat/handle/10803/128504.
[39] C. Amaris, M. Bourouis, M. Vallès, Effect of advanced surfaces on the ammonia absorption process with NH3/LiNO3 in a tubular bubble absorber, Int. J. Heat Mass Tran. 72 (2014) 544–552, https://doi.org/10.1016/j.ijheatmasstransfer.2014.01.031.
[40] ANSYS, ANSYS fluent theory guide, New York, USA. https://doi.org/10.1016/0140-3664(87)90311-2, 2013.
[41] W.M.H.K. Versteeg, An Introduction to Computational Fluid Dynamics. The Finite Volume Method, 1st ed., New York, 1995.
[42] S. Libotean, A. Martín, D. Salavera, M. Valles, X. Esteve, A. Coronas, Densities, viscosities, and heat capacities of ammonia + lithium nitrate and ammonia + lithium nitrate + water solutions between (293.15 and 353.15) K, J. Chem. Eng. Data 53 (2008) 2383–2388, https://doi.org/10.1021/je8003035.
[43] S. Libotean, D. Salavera, M. Valles, X. Esteve, A. Coronas, Vapor-liquid equilibrium of ammonia + lithium nitrate + water and ammonia + lithium nitrate solutions from (293.15 to 353.15) K, J. Chem. Eng. Data 52 (2007) 1050–1055, https://doi.org/10.1021/je7000045.
[44] Y. Cuenca, D. Salavera, A. Vernet, A.S. Teja, M. Vallès, Thermal conductivity of ammonia + lithium nitrate and ammonia + lithium nitrate + water solutions over a wide range of concentrations and temperatures, Int. J. Refrig. 38 (2014) 333–340, https://doi.org/10.1016/j.ijrefrig.2013.08.010.
[45] W. Haltenberger, Enthalpy-concentration charts from vapor pressure data, Ind. Eng. Chem. 31 (1939) 783–786, https://doi.org/10.1021/ie50354a032.
[46] L.A. McNeely, Thermodynamic properties of aqueous solutions of lithium bromide, Build. Eng. 85 (1979) 413–434.